ORIGINAL PAPER

Synthesis of Cu-doped NiO thin films for supercapacitors applications: experimental and first principles analysis

Fathi Messaoudi[1,2] · Elhadj Benrezgua[3,4] · Noudjoud Lebga[1,5] · Smail Terchi[3,6] · Mohamed Redha Khelladi[2,7] · Imene Abid[7] · Abderrahim Siassi[1,2] · Bahri Deghfel[3,8] · Abdelhamid Guelil[9] · Abdelhalim Zoukel[10] · Abdelhalim Kahoul[1,2] · Salim Daoudi[1,2] · Ahmad Azmin Mohamad[11]

Abstract

Thin films of pure NiO and Cu doped NiO (CNO) were synthesized using the sol–gel spin-coating route. All samples exhibited a cubic phase with a predominant orientation along the (200) axis, which relaxed with Cu doping. Surface morphology showed an increase in grain size with molarity (36.20–129.9 nm), resulting in a rougher surface texture with a smoother and more uniform surface after Cu doping (*Rrms*: 91.30–13.80 nm), leading to a decrease in average transmittance and a slight reduction in band gap energy (E_g: 3.62–3.56 eV). The structural, electronic and optical properties of NiO and CNO structures were analyzed by implementing the density functional theory corrected by the Hubbard approach (DFT+GGA+U). The study highlighted the coexistence of ionic and covalent bonding. The DFT+GGA+U method allowed a notable improvement in the calculated E_g (3.57 eV for x=0% and 3.55 for 6.25%), revealing a decrease in E_g with Cu doping. The dielectric functions showed three main peaks, while the static dielectric constants underwent minor variations in response to Cu doping. Electrochemical analysis revealed n-type behavior, high energy efficiency (88%), and specific capacitance up to 37.8 $F.g^{-1}$, confirming the suitability of CNO/ITO electrode for supercapacitor applications.

✉ Elhadj Benrezgua
elhadj.benrezgua@univ-msila.dz

Ahmad Azmin Mohamad
aam@usm.my

1 Laboratory of Materials Physics, Radiation and Nanostructures (LPMRN), Faculty of Sciences and Technology, University of Mohamed El Bachir El Ibrahimi, 34030 Bordj-Bou-Arreridj, Algeria

2 Department of Matter Sciences, Faculty of Sciences and Technology, Mohamed El Bachir El Ibrahimi University, 34030 Bordj-Bou-Arreridj, Algeria

3 Laboratory of Materials and Renewable Energy, Faculty of Sciences, University of M'sila University Pole, Road Bourdj Bou Arreiridj, 28000 M'sila, Algeria

4 Department of Natural and Life Sciences, Faculty of Sciences, University of M'sila University Pole, Road Bourdj Bou Arreiridj, 28000 M'sila, Algeria

5 Department of Physics, Faculty of Sciences, University of Setif 1, 19000 Setif, Algeria

6 Faculty of Science, Department of Chemistry, University Mohamed BOUDIAf M'Sila, University Pole, Road Bourdj Bou Arreiridj, 28000 M'sila, Algeria

7 Laboratoire de Chimie Ingénierie Moléculaire Et Nanostructure (LCIMN), Université Ferhat Abbas Sétif-1, Setif 19000, Algérie

8 Department of Physics, Faculty of Sciences, University of M'sila University Pole, Road Bourdj Bou Arreiridj, 28000 M'sila, Algeria

9 Department of Chemistry, Faculty of Sciences, University of Biskra, Biskra, Algeria

10 Laboratory Physico-Chemistry of Materials, Laghouat University, Laghouat, Algeria

11 Energy Materials Research Group (EMRG), School of Materials and Mineral Resources Engineering, Universiti Sains Malaysia, 14300 Nibong Tebal, Pulau Pinang, Malaysia

Introduction

Nickel oxide (NiO) emerges as a material of p-type semi-conducting oxide with a broad band gap ranging from 3.6 eV to 4 eV [1]. NiO adopts a NaCl-like structure with octahedral coordination of Ni(II) and O^{2-} ions [2]. The exceptional properties of NiO make it highly promising for diverse applications, including catalysts, chemical sensors, antiferromagnetic materials, electrochromic devices, supercapacitor applications like other metal oxides (MnO_2 [3, 4]) and carbon materials [5]. These studies were preceded by other investigations on supercapacitors that focused on rigid, flexible capacitors and dye-sensitized solar cells [6, 7]. In recent years, doping NiO with various elements such as Cu, Fe and Au has gained significant attention due to its impact on the optical, electronic, and magnetic properties [8]. Few studies have shown that Cu-doping in NiO (CNO) alters the crystal structure, reducing it towards an amorphous phase, while also decreasing the energy band gap [8, 9]and weakening ferromagnetism [10].

Numerous studies have investigated nickel oxide (NiO) thin films for supercapacitor applications, focusing on compositional tuning through doping strategies, including copper incorporation, to enhance electrochemical properties [11–13]. While most works emphasize doping, limited attention has been given to the influence of precursor molarity in spin-coating techniques, despite its critical role in preserving structural integrity, optical transparency, and electrical conductivity, as well as minimizing defect formation in NiO films [14]. Given its high theoretical capacitance, excellent chemical stability, and low production cost, NiO continues to stand out as a strong candidate for supercapacitor electrode applications [15]. Supercapacitor electrodes can be classified into two types based on their energy storage mechanism: electrochemical electrodes and double-layer electrodes [16]. Copper-doped NiO (CNO) has demonstrated superior electrochemical behavior, making it a key material for enhancing energy storage performance [17].

To complement experimental investigations, density functional theory (DFT) serves as a powerful theoretical approach for understanding the fundamental mechanisms governing the electronic, structural, and optical properties of NiO and its doped counterparts. DFT is a valuable tool for exploring the electronic, structural, and optical properties of NiO and doped variants used in supercapacitors [18]. However, standard DFT approaches such as LDA and GGA often struggle with accurately modeling systems containing strongly correlated d or f electron s [19], like NiO. To overcome these limitations, methods such as LDA+U, which incorporates on-site Coulomb interactions via the Hubbard model, have been developed [20]. This hybrid approach improves the treatment of localized d-states while retaining conventional DFT accuracy for itinerant electrons, enabling more reliable theoretical predictions and optimization of NiO-based supercapacitor materials [21].

Unlike previous Cu–NiO studies focused mainly on dopant concentration [22, 23], this work investigates the role of precursor molarity in spin-coated films, demonstrating its critical impact on morphology, defect density, and electrochemical response. Moreover, the incorporation of DFT+U analysis provides a deeper understanding of Cu-induced electronic modifications, offering a complementary theoretical perspective rarely combined with experimental optimization in NiO-based supercapacitor studies.

In this work, CNO thin films were fabricated by varying Cu in NiO ($x = 6.25\%$). The thin films were characterized in terms of their electronic, optical, structural, and morphological properties. Theoretical calculations were performed using the DFT-GGA+U method in order to predict the characteristics of NiO and CNO structures, to be compared then with experimental values. Electrochemical performance was evaluated through cyclic voltammetry (CV) and galvanostatic charge–discharge (GCD) measurements.

Experimental

Synthesis and characterization of Cu doped NiO

Nickel acetate tetrahydrate ($Ni(CH_3COO)_2 \cdot 4H_2O$), copper chloride ($CuCl_2$), monoethanolamine (MEA), and ethanol were utilized as the starting precursor, dopant source, stabilizer, and solvent, respectively, to prepare NiO an CNO thin films by the of sol–gel spin coating method on glass substrates. The metal ions concentration was varied at 0.4 M, 0.6 M, and 0.8 M. A most suitable molarity of 0.8 M, which yielded high crystallinity, was selected for Cu doping at concentration of $x = 6.25\%$. The molar ratio of metal ions to MEA was maintained at 1.0. The solution was aged at room temperature for 24 h and stirred at 65 °C for 2 h. Using a spin coater, the sol–gel was dropped into a dry and clean substrate (using deionised water and an ultrasonic cleaner) at 2800 rpm for 30 s. The film was then preheated for 10 min at 250 °C to remove organic residues and evaporate the solvent. The preheating and coating procedures were carried out multiple times. The films were ultimately annealed for 1.5 h at 450°C. The precursors were also combined in different molar ratios to obtain the required amount of Cu dopant. The electrochemical performance was evaluated using CV and GCD measurements, carried out in a three-electrode configuration with the working electrode CNO thin film prepared on an indium tin oxide (ITO)-coated glass substrate, a platinum wire as the counter electrode and an

Ag/AgCl electrode as the reference, using a 0.1 M Na_2SO_4 electrolyte.

The structural properties of NiO and CNO thin films were investigated using X-ray diffractometer (XRD; Bruker D8 Advance, $2\theta = 5.0500° - 89.9500°$, step size: 0.1000°, scan step time: 0.8800 s, Continuous scan mode, Cu-Kα: $\lambda = 1.5406$ Å). The surface morphology was examined through atomic force microscopy (AFM: MFP-3D CAR) with the microscopy of scanning electron and energy dispersive X-ray spectroscopy (EDS) (Quattro ESEM, USA). Fourier-transformed infrared spectroscopy (FTIR; Perkin-Elmer System 2000 spectrometer, USA) has been conducted in the spectra range 4000–400 cm^{-1}. The optical transmission spectra were also recorded in the range of 300–800 nm utilizing a UV–Vis spectrophotometer (UV-3101 PC, Shimadzu).

Computational calculation

DFT computations, as implemented in CASTEP code, were executed to investigate the electronic, magnetic, structural and optical properties of NiO and CNO. Meta-GGA (generalized gradient approximation) DFT-RSCAN functional is used to treat the exchange–correlation function [24]. The substitution technique and the optimized primitive NiO cell (Fig. 1a; space group Fm-3 m: 225) were used to construct a conventional rock salt-type NiO cell (Fig. 1b), leading to building a $2 \times 2x2$ NiO supercell (Fig. 1c). To achieve a Cu content of x = 6.25%, one Ni atom was substituted with Cu in the $2 \times 2 \times 2$ supercell, as shown in Fig. 1c. The kinetic energy cut-off of 571.4 eV was applied for the plane-wave ultrasoft pseudopotential method generated on the fly (OTFG) [25]. Gamma centered grid of $5 \times 5 \times 5$ and $3 \times 3 \times 3$ k-point is used for the conventional cell and $2 \times 2 \times 2$ supercell, respectively. The valence-electron configurations for the Ni ($3d^9 4s^1$), O ($2s^2 2p^4$) and Cu ($3d^{10} 4s^1$) were selected. The convergence criteria are 0.03 eV/for maximum force, 10^{-3}Å for maximum displacement, 1.0×10^{-5} eV/atom for energy change, 0.05 GPa for maximum stress, and 1.0×10^{-6} eV per atom for self-consistent field (SCF) threshold. The semiempirical GGA + U approach was used and the effective

Hubbard U values were set at 10 eV for Ni 3 d,8 eV for O 2p, and 10 eV for Cu 3 d states. The chosen U values were adopted from previously reported literature on transition-metal oxides to ensure consistency with earlier studies [8, 15, 20, 24]. The NiO and CNO antiferromagnetic phase, consistent with prior reports, was adopted [25].

Results and discussion

Experimental results

Crystallographic analysis of the deposited films confirmed the formation of a single-phase cubic rock-salt structure, characteristic of NiO (JCPDS 73–1519), devoid of secondary impurities. The diffraction patterns (Fig. 2) exhibited intense reflections corresponding to the (111), (200), and (220) planes. Rietveld refinement, performed using HighScore Plus [26, 27], indicated a lattice parameter of a = 4.1829 Å, which aligns well with standard values. The sharpness of the diffraction peaks across all precursor concentrations attests to the high crystallinity of the synthesized films, with a distinct preferential growth along the (200) direction. The lattice parameter value does not change significantly, as the atomic radii of Ni and Cu are very close and all the films exhibit an average thickness of approximately 400 nm which is comparable to those reported previously [28, 29]. XRD measurements revealed slight peak shifts and lattice distortions consistent with the substitution of Ni^{2+} by Cu^{2+} ions.

The preferential orientation was quantitatively assessed using the texture coefficient (TC) formalism [30]. Analysis revealed TC(200) values exceeding unity, confirming that the (200) plane represents the thermodynamically favored growth direction. Regarding the microstructural evolution, an elevation in precursor molarity promoted grain growth, increasing the crystallite size from ~ 31 nm to ~ 46 nm (Fig. 2c), a behavior consistent with solution-processed oxide films [31]. Conversely, Cu incorporation interrupted this trend, reducing the crystallite size to 40.79 nm. This shrinkage is attributed to the ionic radius mismatch between

Fig. 1 (**a**) NiO primitive cell, (**b**) NiO conventional cell, and (**c**) $2 \times 2x2$ NiO supercell; nickel (Ni) atoms are denoted by blue color and oxygen (O) atoms are denoted by red color and copper (Cu) atoms are denoted by brown color
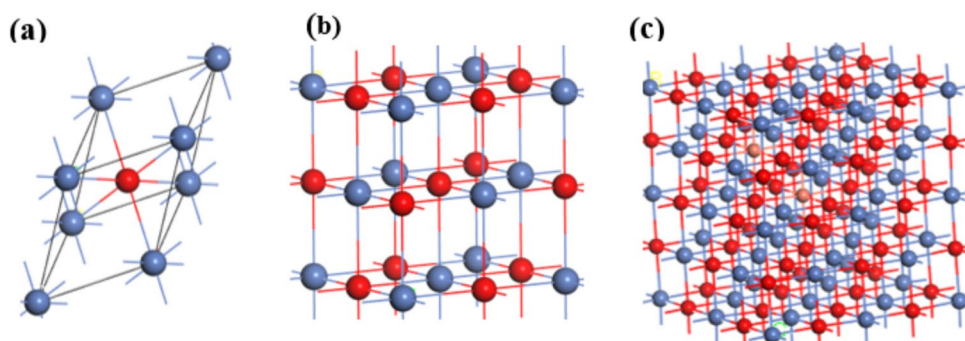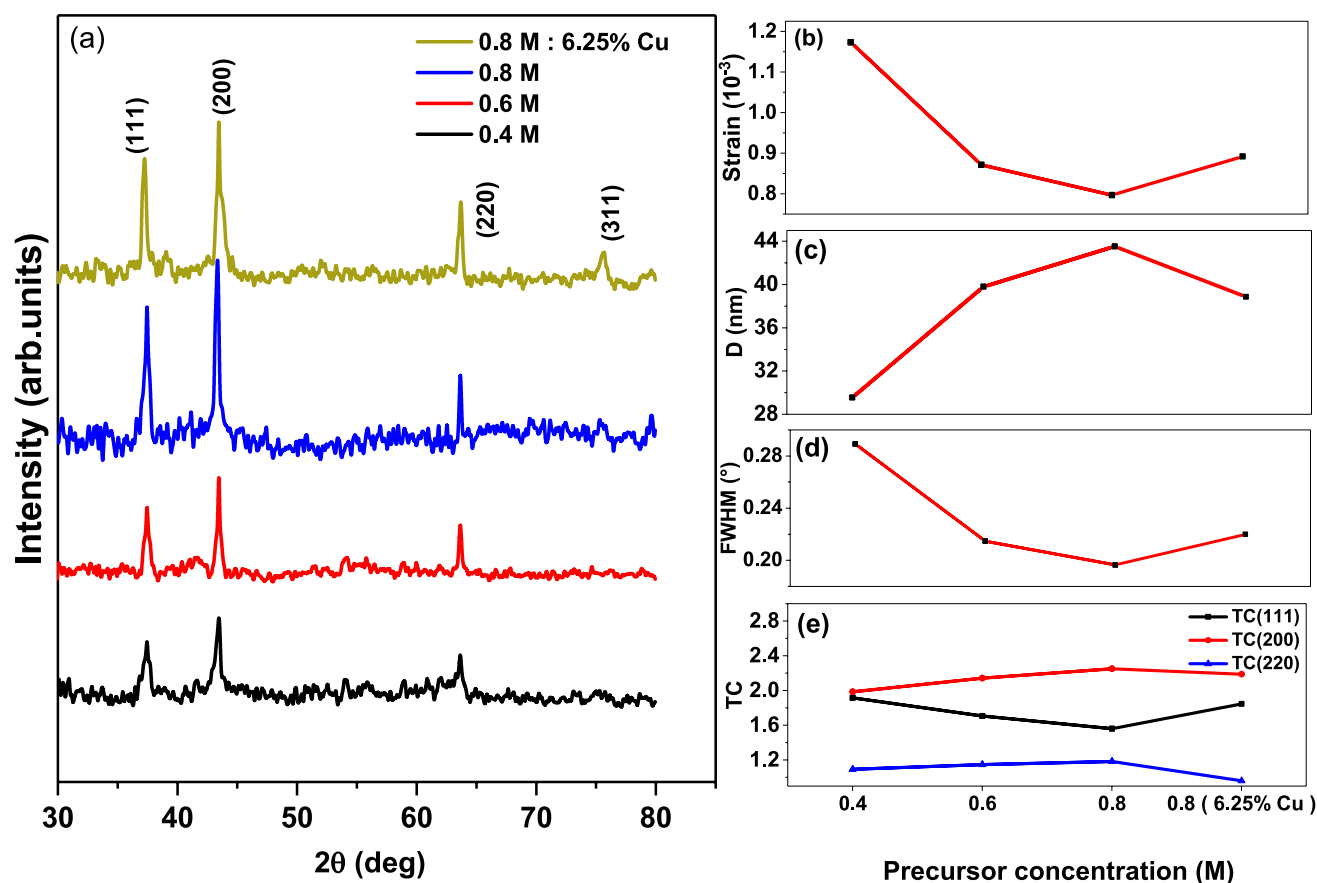
Fig. 2 (**a**) XRD Patterns, (**b**) strain variation, (**c**) crystallite size variation, (**d**) *FWHM* variation and (**e**) *TC* (hkl) variation of NiO thin films and CNO thin films (0.4 M, 0.6 M,0.8 M, and 0.8 M with 6.25% Cu)

Ni^{2+} (0.78 Å) and Cu^{2+} (0.96 Å), which generates lattice stress and inhibits grain boundary coalescence [32]. This reduction is further supported by the decreased intensity of the (200) XRD peak after Cu doping, indicating a decline in film crystallinity (Fig. 2a). The enhancement in the crystalline structure of NiO thin films with increased precursor molarity refers to the higher distribution of Ni species on the glass substrate surface.

Micro-strain analysis (Fig. 2b) indicated a relaxation of lattice defects with increasing precursor concentration (0.4 M, 0.6 M, 0.8 M NiO), whereas Cu doping reintroduced lattice strain [28, 29]. 2D pictures of ITO substrate, NiO (0.4 M, 0.6 M, 0.8 M) and CNO thin films are shown as samples of presentation (Fig. 3a, b, c, d, e). 50 X 50 μm² 2D and 3D AFM images are presented for NiO and CNO thin films (Fig. 3f, g, h, i). The grain shapes are generally round, and their medium average size rises with molarity. However, a significant decrease in grain size is observed after 6.25% Cu doping (Table 1). This finding agrees with the increase that occurs in (200) preferential orientation. Hence, the a-axis grain growth as the molarity rises. The surface becomes rougher with an increased level of molarty

and becames smooth after Cu doping. This morphology is compatible with the average grain size values (Table 1).

The surface morphology (SEM) and elemental composition (EDS) of NiO and CNO thin films were further characterized at 10 k magnification (Fig. 4a). The surface morphology of the deposited NiO and CNO thin film appears quasi smoothly with spherical grains (Fig. 4a,b). Uniform surfaces with closely packed spherical particles reflect the high quality of the prepared film [33]. CNO exhibits more pronounced voids and cracks, suggesting that Cu ion incorporation influences the surface morphology [34]. EDS analysis confirms the presence of oxygen (O) and nickel (Ni) in both samples, with the appearance of copper (Cu) peaks for CNO thin films (Fig. 4b). Furthermore, it is obtained from the quantitative examination that the Cu concentration of 5.6% corresponds with the actual Cu content of 6.25% incorporated during the preparation (inset in Fig. 4b), attesting to the successful doping.

The variations in optical properties are primarily influenced by the changes in the crystallite size, specifically, the increase in the band gap energy due to a reduction in crystallite size [35]. The transmittance of NiO and CNO thin
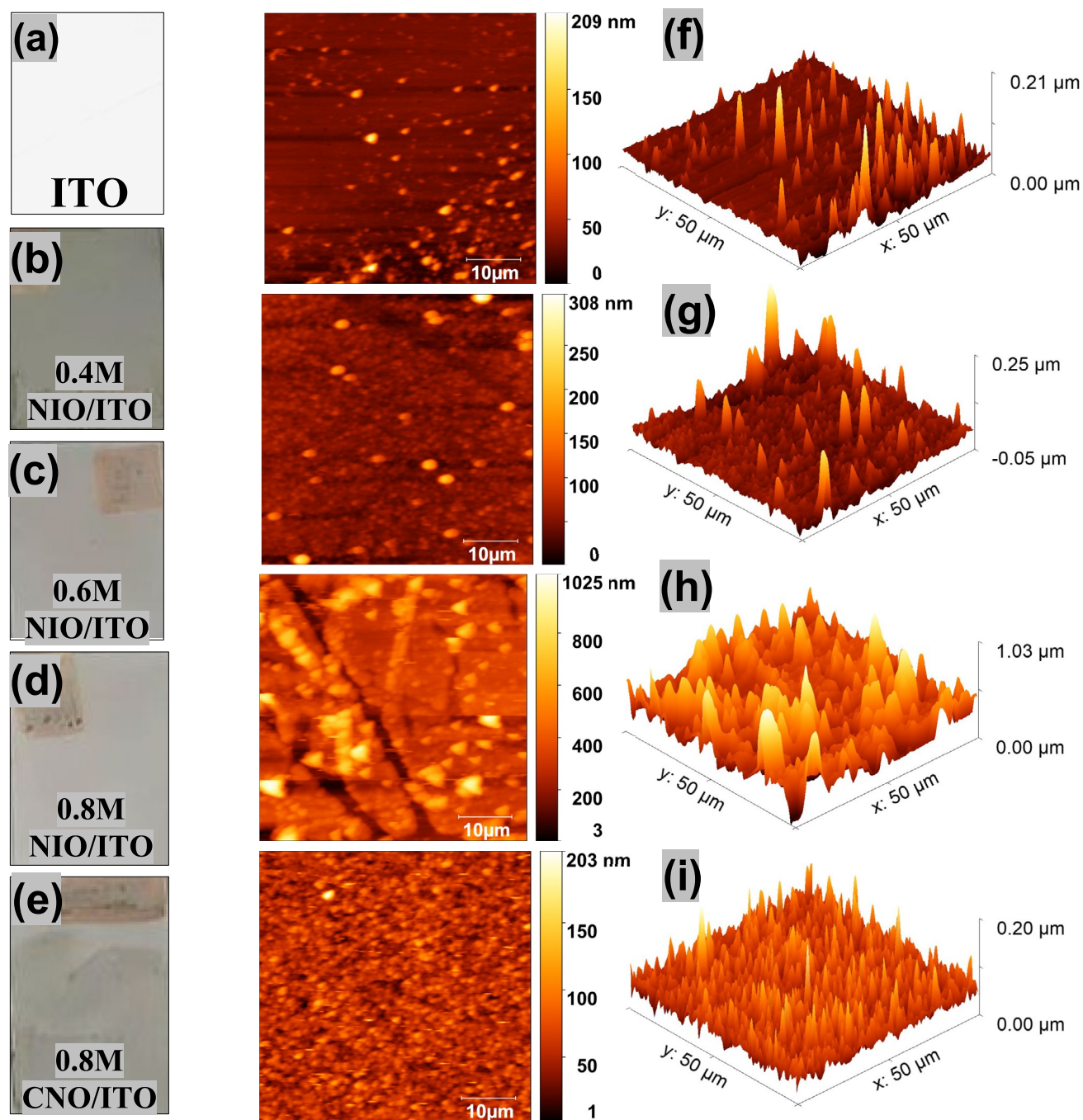
Fig. 3 2D pictures of (**a**) ITO substrate, NiO (**b**) 0.4 M, (**c**) 0.6 M, (**d**) 0.8 M and CNO (**d**) thin films samples fabricated by sol–gel spin coating process at laboratory scale. AFM images of 50 X 50 μm² 2D and 3D; NiO along with CNO thin films (**f**) 0.4 M, (**g**) 0.6 M, (**h**) 0.8 M and (**i**) 0.8 M:6.25% Cu

Table 1 Structural and morphological parameters of NiO and CNO films ($x = 6.25\%$)

Molarity (M)	2θ (°)	a (Å)	FWHM (°)	Peak intensity	Crystallite size (nm)	Grain size (AFM) (nm)	$Rrms$ (nm)
0.4	43.397	4.165	0.289	(200)	30.90	36.20	16.69
0.6	43.373	4.167	0.214	(200)	41.73	59.14	45.22
0.8 ($x = 0.0\%$)	43.349	4.165	0.196	(200)	45.56	129.9	91.30
0.8 ($x = 6.25\%$)	43.445	4.160	0.219	(200)	40.79	49.54	13.80
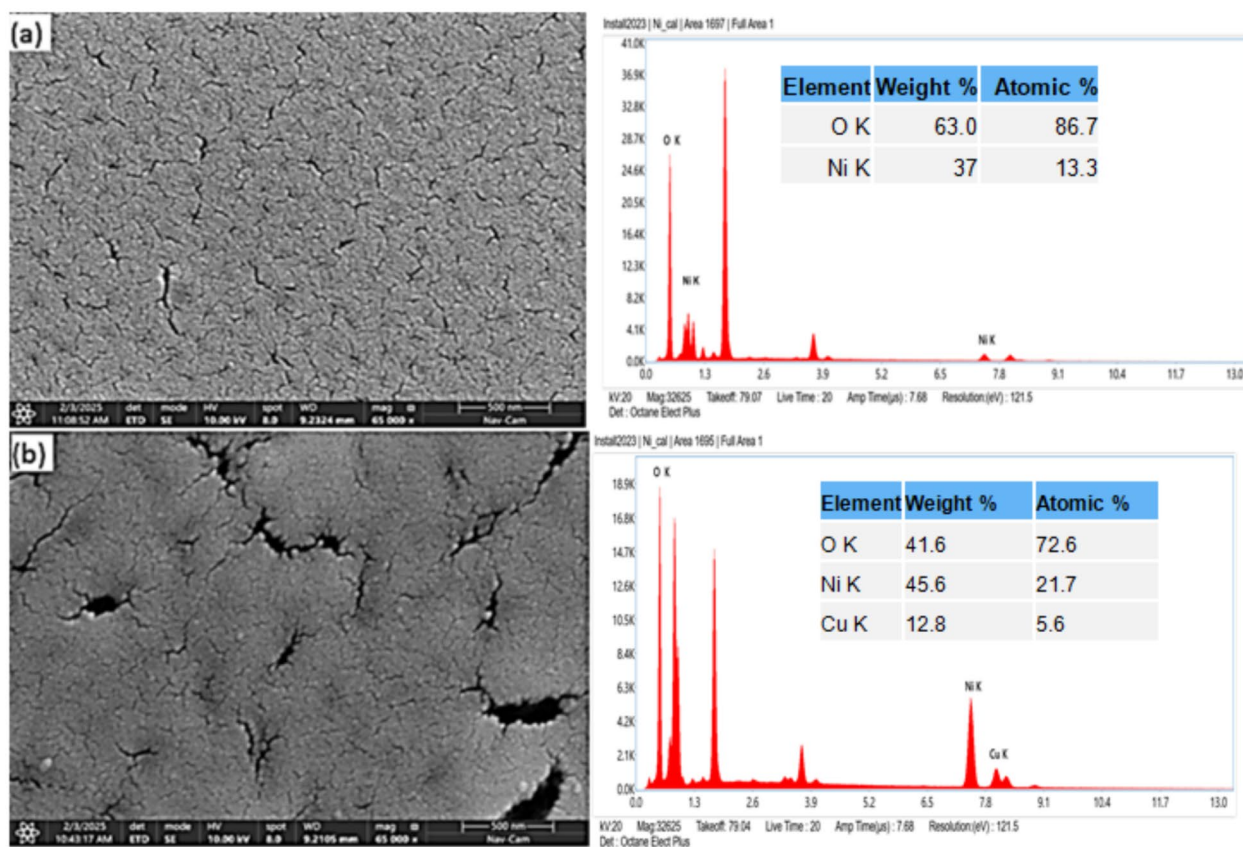
Fig. 4 SEM images and EDX spactra of (**a**) NiO (0.8 M) and (**d**) CNO thin films (0.8 M: 6.25% Cu). Accelerating voltage: 10.000 kV, Magnification: 65 000 x, Working distance for SEM: 9.2105 mm, Calibration standards used for EDS analysis: Fe

films decreases from 80 to 70% with increasing molarity (Fig. 5a). Similar results have been previously reported for NiO thin films via sol–gel technique [36]. This can be attributed to the growth of the grain size which leads to a decrease in grain boundary density or in the number of scattering centers. The absorption maximum wavelength of NiO thin films are demonstrated to rely on their particle size and generally decreases with particle size reduction [35].

The relation of Tauc, $(\alpha h v)^n = A(h v - E g)$ was used to compute the optical band gap (Eg) of the nanoparticles [37], where α is the absorption coefficient [38], $h v$ is the energy of photon, A is the band tailing parameter, Eg is the bandgap energy and $n = 1/2$ corresponds to indirect electronic transitions [39]. The Eg is computed by extrapolating the linear region of the $(\alpha h v)^{1/2}$ vs. $h v$ to the energy axis at $(\alpha h v)^{1/2} = 0$, as indicated in the inset of Fig. 5b. The calculated Eg ranges from 3.56 to 3.62 eV, which is consistent with values previously reported in the literature for NiO thin films [40, 41]. These calculated values show a gradual decrease in Eg with increasing molarity (Table 2) [42]. The sharp UV absorption edge shifts slightly to longer wavelengths upon Cu doping, reducing E_g from 3.57 eV to 3.56 eV (Table 2). This reduction is in agreement to the findings reported for Cu-doped

NiO thin film [43]. Additionally, improving the crystallinity and reducing crystal defects can be responsible for Eg decrease in CNO thin films [28].

The optical parameters including the absorption coefficient α, the extinction coefficient k, the refractive index n, the imaginary part ε_2 and the real part of the dielectric function be calculated from the transmittance and the absorbance (Fig. 5b, c, d).

Fundamental optical constants were derived from the transmittance spectra using standard relations involving film thickness [44]. The extinction coefficient (k), representing light attenuation, was evaluated for normal incidence [24], while the refractive index (n) was determined as a function of wavelength [45]. Consequently, the real ε_1 and imaginary ε_2 parts of the complex dielectric function were established [24]. As depicted in Figs. 5b and 5c, both the dielectric function and refractive index exhibit an ascending trend with photon energy in the visible range (2–3.5 eV), Above this range, both values decrease as the photon energy further increases, which can be attributed to the growth in crystallite size.

The absorption coefficient exhibits an exponential increase with photon energy below the optical band gap Eg,
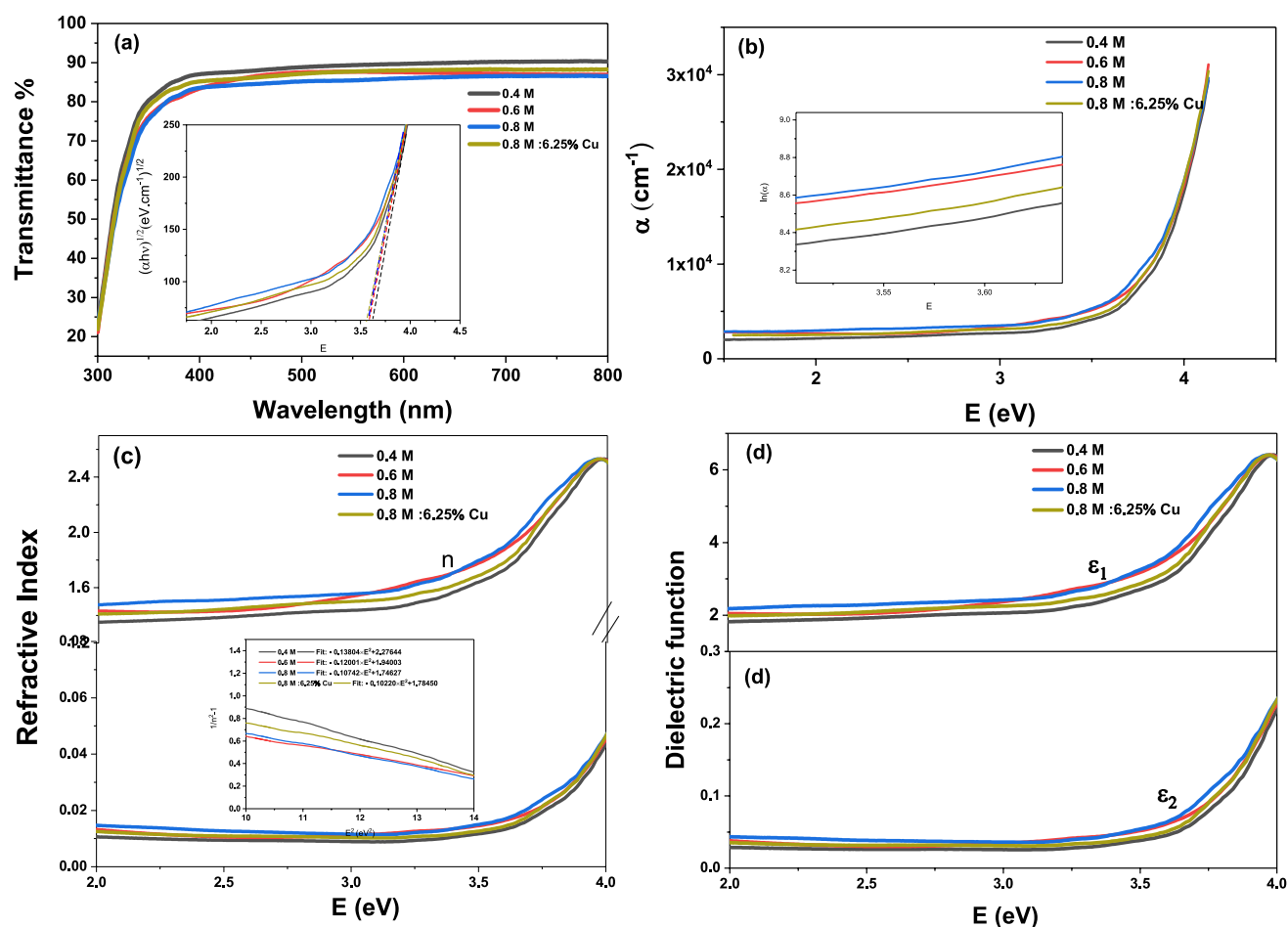
Fig. 5 (**a**) Optical transmission spectra, (**b**) absorption coefficient, (**c**) complex refractive index (**d**) dielectric function of NiO (0.4 M, 0.6 M, and 0.8 M) and CNO, (0.8 M, Cu 6.25%) thin films. Inset in (**a**) dem-onstrates $(\alpha h v)^2$ versus hv and Eg. Inset in (**c**) represents $1/(n^2-1)$ versus E^2. Insect in (**b**) denotes $ln(\alpha)$ versus E

Table 2 Optical criterion of pure NiO and CNO cubic phases ($x = 6.25\%$)

Molarity (M)	Eg (eV)	Ed (eV)	E_0 (eV)	$\varepsilon_0(n_0)$	Eu (eV)
0.4	3.622	3.002	4.641	1.64 (1.28)	0.571
0.6	3.587	3.109	4.619	1.67 (1.29)	0.787
0.8 Pure	3.576	4.966	5.688	1.87 (1.36)	0.814
0.8($x = 6.25\%$)	3.560	5.443	5.858	1.92 (1.38)	0.816

a behavior that is characteristic of the so-called Urbach tail associated with disorder-induced localized states in the band-gap region. This exponential absorption edge leads to a slight effective narrowing of Eg between the valence (Ev) and conduction (Ec) bands. The corresponding Urbach energy Eu, which quantifies the width of the band tail and thus the degree of structural disorder, is obtained from the linear part of the $ln(\alpha)$–photon-energy plot, as shown in the inset of Fig. 5d [46, 47]. The extracted values of Eg and Eu as a function of precursor molarity are summarized in Table 2, and they are consistent with previously reported data for NiO thin films [31].

Figures 5b and c depict the dependence of the optical parameters α, k, n, ε_1, and ε_2 on photon energy $E = hv$. In the sub-band-gap region ($E < E_g$), the dispersion of the refractive index was analyzed using the Wemple–DiDomenico single-oscillator formalism, expressed by Eq. (3), which is widely employed to model the energy dependence of n in dielectric materials [48]. In this approach, a linear fit of $(n^2-1)^{-1}$ versus E_2 (inset of Fig. 5c) allows the determination of the static refractive index n_0 as E approaches 0, together with the oscillator energy E_0, the dispersion energy Ed, and the static dielectric constant $\varepsilon_0 = (n_0)^2$ for NiO and CNO thin films (Table 2). Here, the intercept of the fitted line is related to the ratio $E0/Ed$, while the slope is proportional to $-1/(E0Ed)$ [48].

The α coefficient remains unchanged with increasing E across all films up to the edge of optical absorption). Beyond this point, the absorption coefficient rises sharply and shifts towards lower energy values with varying molarities, suggesting a reduction in E_g. The refractive index increases with energy in the visible light spectrum and shows sensitivity
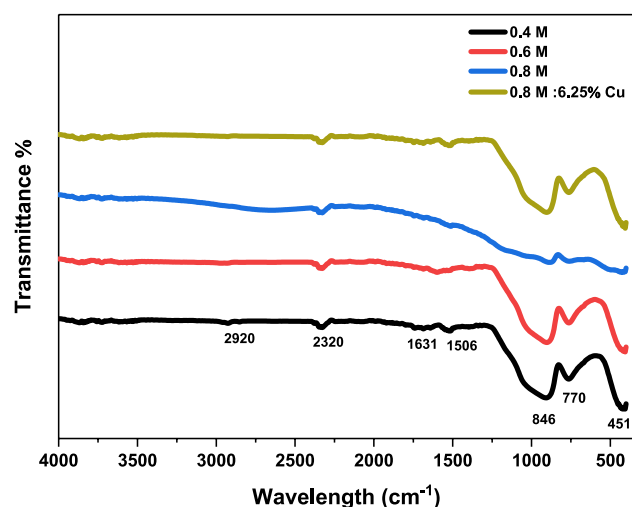
Fig. 6 FTIR scales of pure NiO and CNO fine films (0.4 M, 0.6 M,0.8 M and 0.8 M (6.25% Cu)

to changes in precursor concentration. Furthermore, n_0 increases with molarity, likely due to a reduction in the density of the film induced by the increase in crystallite size (Table 2). These results are consistent with those related by other investigators for pure NiO [45]. Moreover, the dielectric function exhibits a similar trend to the refractive index from which it has been derived (Fig. 5b) whereas the optical band gap and disorder vary inversely.

Figure 6 illustrates the FTIR spectroscopy results, offering valuable understanding into the structural and chemical properties of NiO thin films at varying molarities (0.4 M, 0.6 M, 0.8 M) and CNO (0.8 M with 6.25% Cu) thin films. The characteristic Ni–O vibrational bond was observed around 451 cm^{-1}, corresponding to Ni–O stretching modes, confirming the successful formation of the oxide structure [49]. The band near 451 cm^{-1} may indicate Cu–O vibrations, though it overlaps with Ni–O modes. Additionally, residual organics indicated by peaks at 1506 and 2920 cm^{-1} correspond to O–H stretching vibrations [44]. The bands at 1631 cm^{-1} and 2320 cm^{-1} are attributed to chemically adsorbed CO_2 and H–O–H bending vibrations on NiO nanoparticle surfaces, indicating strong interactions between the thin films and atmospheric water and CO_2 [49].

DFT+U computations

The configuration in which Cu atoms has been positioned at a close distance across the O atom corresponds to the most stable (ground) state [50]. The stable configuration will further serve as a basis for analyzing the influence of Hubbard U values on the electronic structure [51]. Moreover, the Hubbard correction significantly enhances the computed E_g.

The lattice constants ($a=b=c$) are slightly reduced after Cu doping (Table 3) and agree well with the experimental values (0.8 M NiO and 6.25% CNO) within a relative error of 1.08% for $a=b=c$ (Table 2). The bond length is slightly influenced by Cu doping, attributed to the corresponding ionic sizes of Ni and Cu.

The band gap theoretical results (3.55 eV for x=6.25% and 3.57 eV for x=0) show strong agreement with the experimental values (0.8 M; NiO and CNO), with a maximum relative deviation of only 0.28%. An indirect band gap is observed for both NiO and CNO (Fig. 7 middle). Cu doping causes a slight narrowing of the band gap, with the top of the valence band primarily originating from Cu 3 d states (Fig. 7 right), a trend also reported in previous studies [18, 52].

The partial density of O 2s, O 2p, Ni 3s, Ni 3d, Cu 3 s and Cu 3d, spining up and down states (PDOS) for NiO and CNO are plotted (Fig. 7 left). The band states of valence, extending down to −10 eV, with a narrower band appearing at −7.8 eV to −9.2 eV for the CNO and pure structures, respectively, primarily include a strong mixture of O 2p and Ni 3d states, with some assistance from Cu3d states in the case of CNO. The downward change of the CB, dominated by Ni4s and Cu3d states, leads to the decrease of Eg after Cu doping. Cu3d states are spread around Fermi level having zero net spin causing the antiferromagnetic behavior of CNO. Cu doping induces a moment of approximately 1 μ_B/ Cu with a negligible contribution from the oxygen atom [18, 52].

The charge density of slices (001) including Ni, O and Cu atoms for NiO (Fig. 8a) and CNO (Fig. 8b) are demonstrated. The yellow color signifies charge accumulation around the oxygen (O) atoms, while the green and blue colors represent regions of charge depletion. The red color represents charge loss in the interstitial region. High electronegativity is associated with an tendency to attract more electrons, (Ni (1.91), Cu (1.8), and O (3.5)), which are in agreement with the average Mulliken atomic and the bond populations (Table 3). The degree of covalent and ionic bonding in pure and CNO is reflected by the variation between the formal ionic charge and the effective valence charge. Covalency rises with Cu doping, leading to more covalent Cu–O bonds

Table 3 Lattice constants, average Mulliken bond and atomic populations, length of bond and effective valence of NiO and Cu-NiO structures (x=6.25%)

x (%)	Atomic Population (e)			Effective valence (e)		Bond Population (e)		Bond length (Å)		$a=b=c$ (Å)
	Ni	Cu	O	Ni	Cu	Ni–O	Cu–O	Ni–O	Cu–O	
0	1.04	-	−1.040	0.96	-	0.500	-	2.150	-	4.039
6.25	1.023	0.881	−1.014	0.977	1.119	0.205	0.200	2.119	2.107	4.228
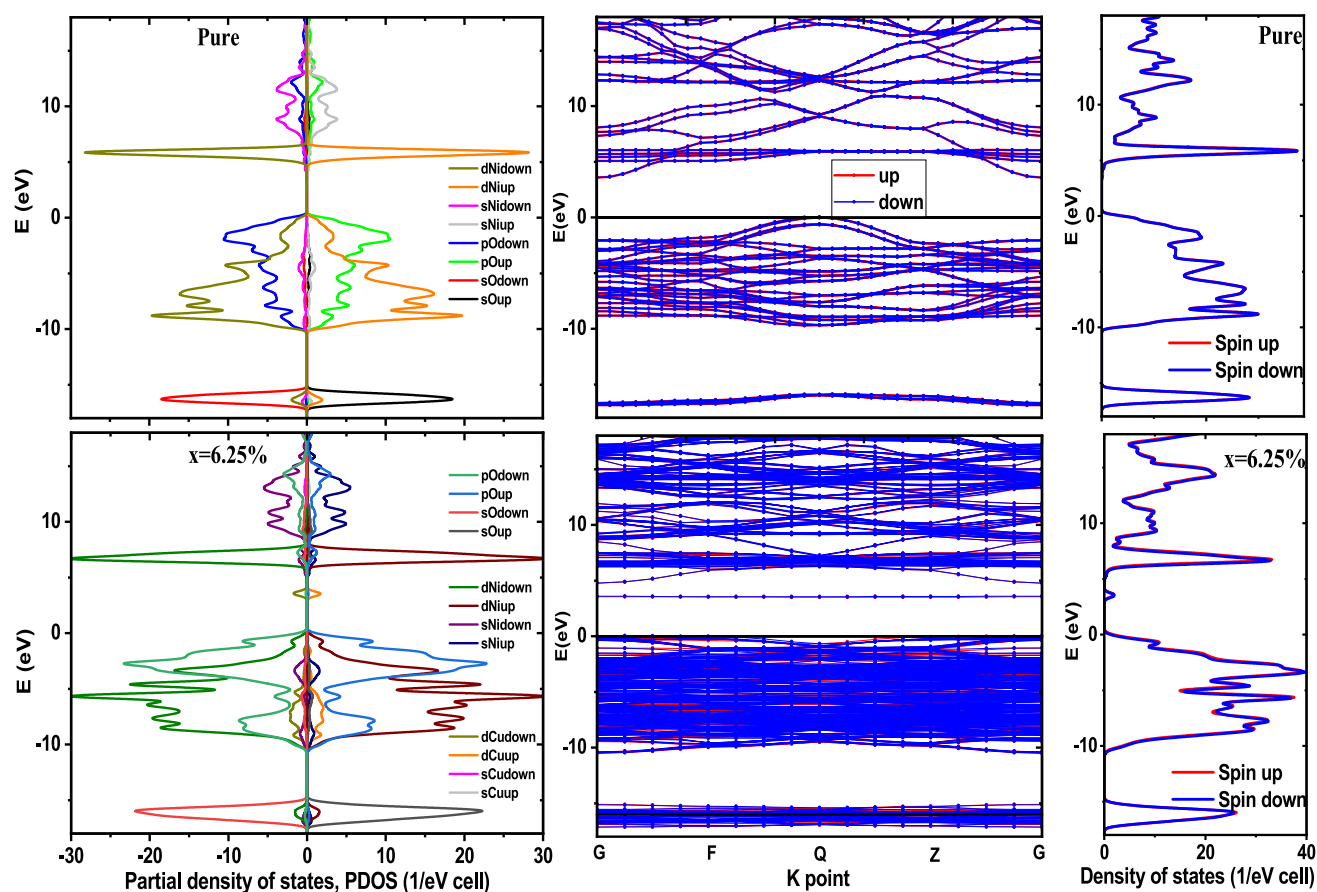
Fig. 7 PDOS of Cu 3 s, Cu 3 d, Ni 3 s, Ni 3 d, O 2p and O 2 s spin down and up states (panel on the left), band structures (panel in the middle), and spin up (red) and spin down (blue) total density (panel on the right) of NiO and CNO ($x = 6.25\%$)

Fig. 8 Electron charge density distribution of (001) surface considering (**a**) NiO and (**b**) CNO rock salt structures
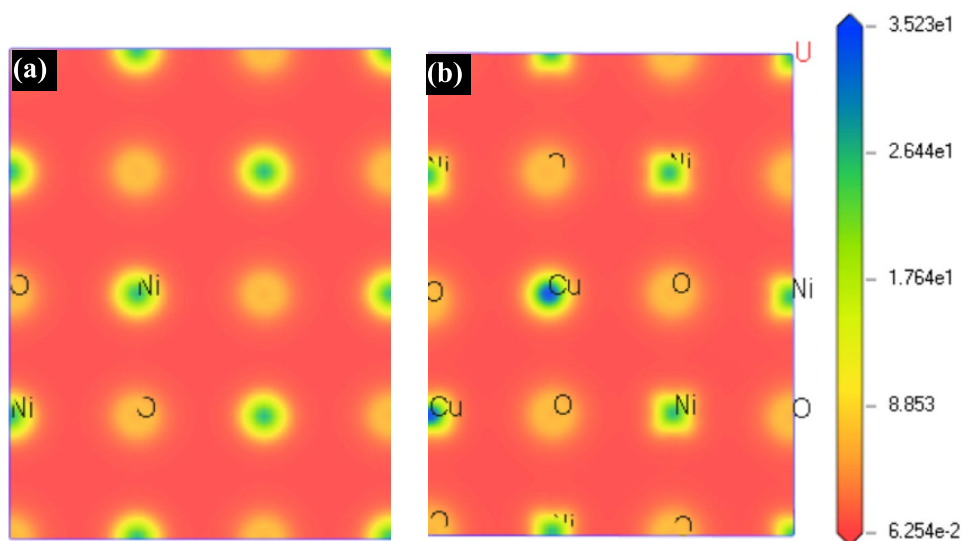
in comparison with Ni–O bonds. The charge density further supports this increase in covalency with Cu doping.

Figure 9a presents the real and imaginary parts of the complex dielectric function for CNO and NiO. The peak around ~8 eV (*Im*. Cu 0%) originates from the electron excitation from the O-2p state to the Ni-3s state. Similarly, the peak around ~9 eV (*Im*. Cu 6.25%) arises from electron excitation from the O-2p state to the Cu-3d state, and its intensity continues unchanged after Cu doping owing to the substitution of Ni by Cu. The peaks at ~12 eV (*Im*. Cu 0%)
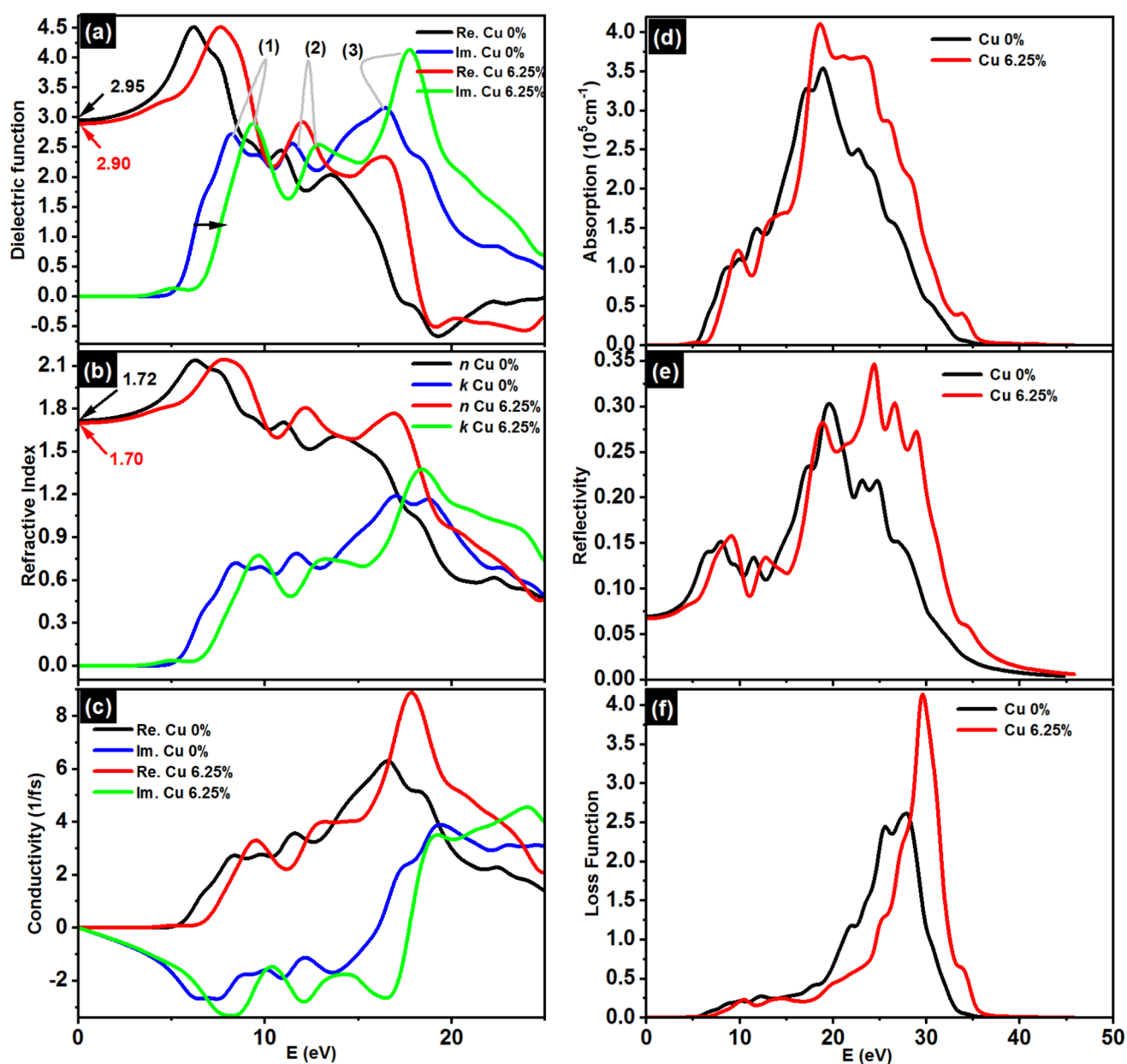
Fig. 9 (**a**) complex dielectric function, (**b**) complex refractive index (**c**) complex conductivity function, (**d**) absorption coefficient, (**e**) optical reflectivity and (f) energy-loss function for NiO and CNO rock-salt phases ($x = 6.25\%$)

and ~ 13 eV (*Im*. Cu 6.25%) are attributed to electron excitation from Ni-*3d* state (near *VB*) to O-*2p* state (near *CB*). The transition from Ni-*3d* state to O-*2 s* state results in strong peaks at approximately 16 eV (*Im*. Cu 0%) and ~ 18 eV (*Im*. Cu 6.25%), which increases after doping owing to the decrease of Ni-*3d* responsible for this shift. A slight red shift in the dielectric function is noticed, referred to the small E_g narrowing for CNO. The constant ε (0) exhibits a small change with x: ε_I (0) = 2.95 for $x = 0\%$ and ε_I (0) = 2.90 for $x = 6.25\%$, which is consistent with experimental results (Table 2). The complex conductivity function, absorption coefficient, complex refractive index, optical reflectivity
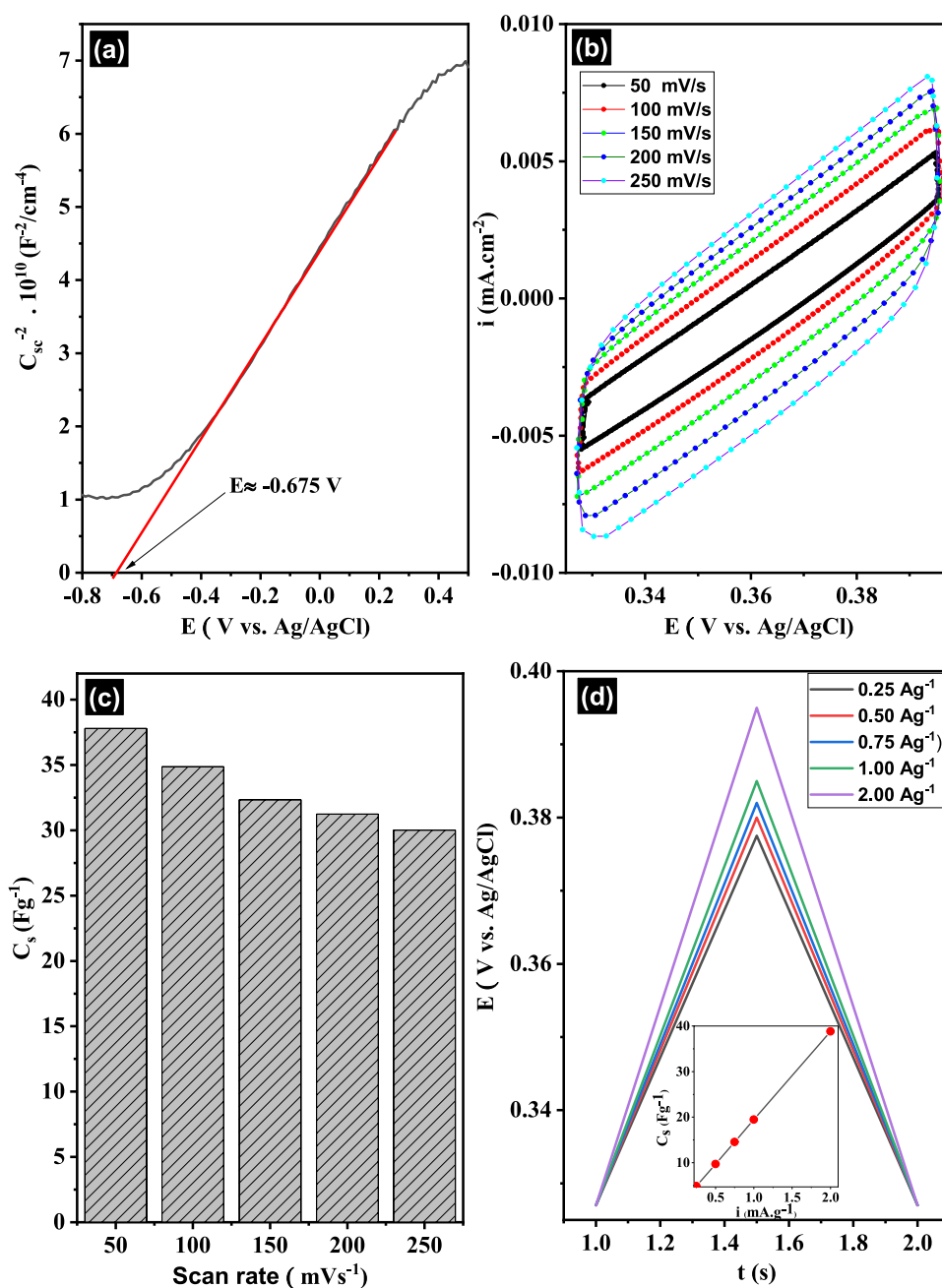
and energy-loss function are also derived (Fig. 9b-f). The absorption shows two strong peaks at ~ 19 and ~ 24 eV. The energy loss function peaks at ~ 29.0 eV for NiO pure and 31 eV for CNO corresponds to sharp decrease in reflectivity. The refractive index decreases slightly from 1.70 to 1.72 at low photon energies after Cu doping, this behavior deviates slightly from experimental observations (Table 2) owing to experimental conditions not taken into account (thickness and surface morphology) in the DFT + LDA + U computations. Additionally, both the refractive index and the absorption coefficient exhibit trends compatible with experimental outcomes within the range of visible energy.

Electrochemical measurement

The comprehensive electrochemical analysis of the CNO/ITO working electrode highlights its strong potential for high-performance supercapacitor applications. For pure and lightly doped metal oxide semiconductors (i.e., non-degenerate), such as NiO with low Cu doping ($\leq 6.25\%$), the standard Mott–Schottky (MS) equation remains valid and can be expressed as [53]:

$$\frac{1}{C_{sc}^2} = \frac{2}{e\varepsilon_0 k N_{sc} A^2}\left(E - E_{fb} - \frac{K_B T}{e}\right) \quad (1)$$

where ε_0 is the vacuum permittivity, C_{sc} is the space-charge region capacitance, k is the static dielectric constant of the thin film ($k = 2.9$),A is the geometric surface area of the CNO electrode ($A = 1 cm^2$) and N_{sc} is the apparent doping density, E_{fb} is the flat-band potential. Figure 10a exhibits the Mott-Schottky plot for CNO thin film prepared on ITO substrate as working electrode. The positive slope of C_{sc}^{-2} vs E plot indicates the CNO is n-type semiconductor. This finding is consistent with previous studies [54, 55], but contrasts with the negative slope reported for NiO thin films in other works [53]. The E_{fb} of the CNO electrode is approximately 0.65 V versus Ag/AgCl reference electrode,

Fig. 10 L(a) Mott-Schottky plot (C_{sc}^{-2} vs. E) of a CNO thin film prepared on ITO substrate at 100 Hz in dark (black) and its corresponding positive slope (red), (b) CV plots of CNO/ITO working electrode at various scan rate, 50, 100, 150, 200 and 250 mVs^{-1} and (c) their corresponding specific capacitance, (d) Charge–discharge plots of CNO/ITO working electrode at various current density, 0.25, 0.5, 0.75, 1 and 2 Ag^{-1} and inset in (d) their corresponding specific capacitance

determined from the intercept of the linear region of the Mott-Schottky plot on the potential axis (E) corrected by the thermal voltage term ($K_B T/e$). The N_{sc} was determined from the slope of the MS plot, yielding a value of 7. 471×10^{20} cm^{-3}. This result is close to the theoretical value (32.89×10^{20} cm^{-3}) and falls slightly outside the typical range reported for CNO in the literature [54, 56, 57]. This high carrier concentration suggests enhanced electronic conductivity and supports efficient charge transport at the electrode–electrolyte interface.

Figure 10b displays the CV curves of CNO/ITO working electrode recorded at scan rates of 50, 100, 150, 200 and 250 mVs^{-1} in the potential range of 0.327–0.395 V. The CV plots exhibit quasi-rectangular shapes across 50–250 mVs^{-1} scan rates, which are characteristic of ideal electrical double-layer capacitor (EDLC) behavior, indicating that the charge storage mechanism is predominantly capacitive. As the scan rate increases, the anodic and cathodic currents rise proportionally, indicating good rate capability and a surface-controlled charge storage mechanism.

The nearly symmetric and undistorted CV curves at all scan rates suggest high reversibility, fast charge–discharge response, and efficient ion transport. These results confirm the excellent electrochemical stability of the CNO/ITO electrode, making it a promising candidate for supercapacitor applications.

The calculated specific capacitance reaches a maximum of 37.8 Fg^{-1} at 50 mV s^{-1}, decreases gradually to 30.01 F g^{-1} at 250 mV s^{-1}, retaining approximately 79% of the initial capacitance and suggests room for improvement through morphological or compositional optimization. This performance, though lower than nanostructured NiO analogues, provides a baseline for further development of doped metal oxide electrodes.

The galvanostatic charge–discharge (GCD) curve of the CNO/ITO electrode (Fig. 10d) exhibits a nearly ideal triangular shape, indicative of good capacitive behavior. At a low current density of 0.25 A g^{-1}, the electrode demonstrates a high energy efficiency of 88%, calculated as the ratio of discharge to charge capacity and slight drops to approximately 80% at 2.0 A g^{-1}, likely due to increased internal resistance and limited ion diffusion at higher charge–discharge rates.

The calculated C_s values increase with the applied current density from 4.85 F g^{-1} at 0.25 A g^{-1} to 38.83 F g^{-1} at 2 A g^{-1}, confirming good capacitive behavior and efficient charge storage. Such behavior indicates better utilization of active sites at higher current densities and possibly enhanced surface wettability or improved ion diffusion dynamics within the electrode material, highlighting the excellent electrochemical performance of the CNO/ITO system for supercapacitor applications. Similar findings have been stated in additional research: a capacitance of 59 F g^{-1} was achieved by the CNO composite electrode at a scan rate of 50 mVs^{-1} [58], NiO nanosheets exhibited specific capacitance values that increased from 28 to 42 F g^{-1} when tested at higher scanning rates [59] and from 182.44 F g^{-1} for NiO to 436.95 F g^{-1} for 10 at% Cu NiO thin films [56].

Figure 11a–c illustrates the EIS and cycling stability analyses of Cu-doped NiO thin films with different deposited layers (C3 and C5, corresponding to 10 and 15 layers, respectively). The Nyquist plots in Fig. 11a exhibit a single semicircle at high frequencies, characteristic of the charge-transfer resistance (Rct). The reduced semicircle diameter for the C5 sample indicates a lower Rct, implying faster electron transport and improved interface contact between the electrode and electrolyte due to enhanced Cu incorporation and increased film thickness. This figure exhibits the same characteristic shape previously described by Yadav et al. [60].

The cyclic voltammetry (CV) profiles in Figs. 11b,c reveal high reversibility and excellent electrochemical stability over 100 continuous cycles in 0.1 M Na$_2$SO$_4$ electrolyte. The nearly overlapping CV curves, along with the negligible decrease in current density, demonstrate the strong adhesion and mechanical integrity of the films. The C5 electrode retains a more symmetric CV shape and higher current response compared to C3, suggesting enhanced redox activity and improved ion diffusion pathways. Overall, the EIS and cycling results confirm that increasing the number of deposited layers (C5) significantly improves the charge transport kinetics and long-term durability of Cu-doped NiO electrodes, positioning them as promising candidates for high-performance supercapacitor applications. This behavior is consistent with the findings of El Nady [61] and Chan [62].

Table 4 provides a comparison between the present study and key literature reports on NiO-based electrodes. While most previous works relied on nanopowder synthesis routes such as spray deposition [63], polymerization [64], hydrothermal processing [65], or chemical precipitation [66, 67], our study focuses on spin-coated thin films whose properties are tuned through precursor molarity. Although earlier reports report specific capacitances between 24 and 52 F/g depending on the method and dopant type, our Cu-NiO thin film demonstrates competitive electrochemical performance under comparable conditions. This confirms that precursor molarity is a critical parameter controlling the morphology, charge-transfer behavior, and overall electrochemical response of Cu-doped NiO systems.

Fig. 11 (**a**) is Nyquist plots of Cu-doped NiO thin films (C3 and C5) fitted with the equivalent circuit model (inset), showing reduced charge-transfer resistance (Rct) for C3 and C5. Applied potential of −0.5 V vs. Ag/AgCl with a 10 mV amplitude, over a frequency range ranging from 0.01 Hz to 100 kHz. (**b**) and (**c**) are CV curves of C5 and C3 electrodes, respectively, recorded over 100 consecutive cycles in 0.1 M Na_2SO_4
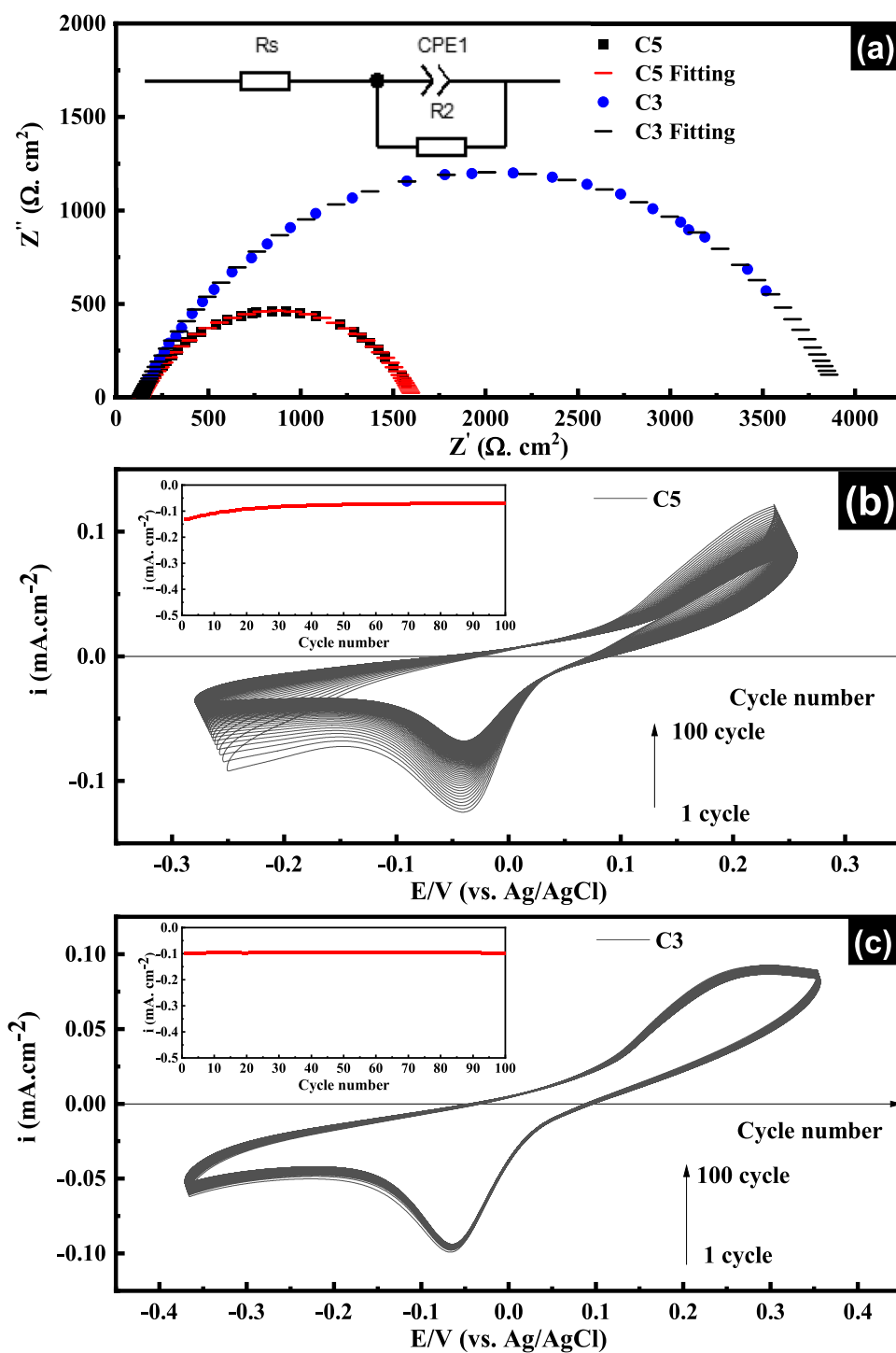
Table 4 Comparison of synthesis methods, electrolyte, and capacitance of NiO -based nanoparticles

Doping element	Synthesis method	Specific capacitance (F/g)	Electrolyte	Ref
Pure/Zr	Spray deposition	24 (at 50 mV/s from CV)	1M KOH	[63]
Pure	Chemical polymerization	41.03 (at 1 A/g from GCD)	2M Na_2SO_4	[64]
Pure	Hydrothermal	30 (at 50mV/s from CV)	1M Na_2SO_4	[65]
Cu	Chemical precipitation	52 (at 50 mV/s from CV)	0.2 M TBACh	[66]
Mn	Chemical precipitation	39 (at 50 mV/s from CV)	2M Na_2SO_4	[67]
Cu	Sol gel	37.8 (at 50 mV/s from CV(	0.1M Na_2SO_4	This Work

Conclusion

Experimental and theoretical examinations were conducted on NiO and CNO thin films. Here are some main highlighted points:

i. All samples demonstrated a cubic rock-salt phase with a predominant (200) orientation. Increasing Ni molarity notably affected the crystallite size, lattice constant and grain size. Cu doping smoothed the surface. The transparency and the energy band gap decreased with increasing molarity and Cu doping. FTIR analysis confirmed successful NiO formation.

ii. GGA+U calculations reveal that Cu doping narrows the band gap, aligning well with experimental results. Antiferromagnetic ground states with stable Cu impurities emerge. Cu 3 d states appear near the Fermi level. Cu–O and Ni–O bonds retain mixed bonding. Dielectric peaks shift slightly; refractive index shows minor Cu sensitivity.

iii. The CNO/ITO electrode exhibited n-type behavior with a flat-band potential of –0.65 V and a donor density of 7. 471×10^{20} cm^{-3}. CV and GCD analyses confirmed excellent capacitive behavior, high reversibility, and energy efficiency up to 88%. The specific capacitance reached 37.8 F/g at 50 mVs^{-1} (CV) and 38.83 F g^{-1} at 2 A g^{1} (GCD), highlighting efficient charge storage and good rate capability, making the CNO/ITO system a promising candidate for supercapacitor applications.

iv. EIS and cycling stability analyses confirmed that optimized Cu doping and increased layer number markedly reduced charge-transfer resistance and enhanced durability. The thicker sample exhibited the lowest Rct, highest current response, and superior cycling stability, confirming its potential as an efficient and durable electrode for supercapacitor applications.

Cu-doped NiO thin films exhibit improved surface uniformity, reduced band gap, and enhanced capacitance, as demonstrated through experimental investigations and DFT+GGA+U calculations. The results highlight the potential of CNO/ITO films for supercapacitor applications, suggesting future research should focus on optimizing doping levels and advancing device integration.

Statement on the use of AI tools:

The manuscript was entirely written by the authors. AI-based tools (ChatGPT) were used only for language refinement and grammar checking, without generating scientific content.

References

1. Devabharathi V, Jagan K, Priyan SR, Vidaarth TN, Surendhiran S, Khadar YS, Kandasamy K (2024) Rational design of NiO nanoflakes and porous GCN nanocomposite for synergic effectiveness on photocatalytic degradation of industry effluents and biological activity. Chem Phys Impact 8:100–637. https://doi.org/10.1016/j.chphi.2024.100637

2. Kannan K, Radhika D, Sadasivuni KK, Reddy KR, Raghu AV (2020) Nanostructured metal oxides and its hybrids for photocatalytic and biomedical applications. Adv Colloid Interface Sci 281:102–178. https://doi.org/10.1016/j.cis.2020.102178

3. Zhu S, Li Y, Zhu H, Ni J, Li Y (2019) Pencil-drawing skin-mountable micro-supercapacitors. Small 15(3):1804037. https://doi.org/10.1002/smll.201804037

4. Aldayyat A, Yam FK (2025) Recent development in metal phosphate-based electrode materials for supercapacitor application: a review. J Solid State Electrochem. https://doi.org/10.1007/s10008-025-06280-7

5. Zhu S, Guan C, Wu Y, Ni J, Han G (2024) Upgraded structure and application of coal-based graphitic carbons through flash joule heating. Adv Funct Mater 34(39):2403961. https://doi.org/10.1002/adfm.202403961

6. Zhu S, Ni J, Li Y (2020) Carbon nanotube-based electrodes for flexible supercapacitors. Nano Res 13(7):1825–1841. https://doi.org/10.1007/s12274-020-2729-5

7. Zhu S, Sheng J, Chen Y, Ni J, Li Y (2021) Carbon nanotubes for flexible batteries: recent progress and future perspective. Natl Sci Rev. https://doi.org/10.1093/nsr/nwaa261

8. Hopoğlu H, Kaya D, Maslov MM, Kaya S, Demir İ, Altuntaş İ, Ungan F, Akyol M, Ekicibil A, Tüzemen EŞ (2023) Investigating the optical, electronic, magnetic properties and DFT of NiO films prepared using RF sputtering with various argon pressures. Phys B 661:414937. https://doi.org/10.1016/j.physb.2023.414937

9. Abdel-wahab MS, El Emam HK, El Rouby WM (2023) Sputtered Ag-doped NiO thin films: structural, optical, and electrocatalytic activity toward methanol oxidation. J Mater Sci Mater Electron. https://doi.org/10.1007/s10854-023-11029-x

10. Bhujel K, Thangavel R, Pal KK, Sardar P, Nayak D, Singh NS, Rai S (2024) Cu-doped NiO thin film's structural, optical, and electrical properties and its negative absorption behaviour in the infra-red region. Physica B. https://doi.org/10.1016/j.physb.2024.416129

11. Bhujel K, Thangavel R, Pal KK, Sardar P, Nayak D, Singh NS, Rai S (2024) Cu-doped NiO thin film's structural, optical, and electrical properties and its negative absorption behaviour in the

infra-red region. Physica B 688:416129. https://doi.org/10.1016/j.physb.2024.416129

12. Kathiravan P, Thillaivelavan K, Viruthagiri G (2024) Influence of Cu-ion doping in NiO NPs and their structural, morphological, optical and magnetic behaviors for optoelectronic devices and magnetic applications. Spectrochim Acta A Mol Biomol Spectrosc 308:123745. https://doi.org/10.1016/j.saa.2023.123745

13. Begum ME, Islam MB, Ara MH, Doris A, Kaiyum MA, Rasadujjaman M (2024) The prospect of spray pyrolyzed pure, Mn-doped, and Zn-doped nickel oxide thin films as TCO material. Heliyon 10(1):e24244. https://doi.org/10.1016/j.heliyon.2024.e24244

14. Almutairi F, Al-Khalli N, Arkook N, Sebhi N, Aida M (2023) Effect of substrate temperature and precursor salt molarities on the nickel oxide physical properties. J Opt 52(2):793–802. https://doi.org/10.1007/s12596-022-01019-3

15. Salleh NA, Mohammad AH, Zakaria Z, Deghfel B, Yaakob MK, Rahiman W, Kheawhom S, Mohamad AA (2024) Microwave assisted synthesis of nickel oxide nanoparticles at different pH via sol gel method: experimental and first-principles investigations. Inorg Chem Commun 164:112415. https://doi.org/10.1016/j.inoche.2024.112415

16. Su Q, Lin C, Xiang M, Wang N, Sun L, Hu W (2024) Remarkable electrochemical performance of holey MXene/graphene hydrogel-based supercapacitor operated at− 60° C in sulfuric acid aqueous electrolyte. J Solid State Electrochem 28(9):3263–3274. https://doi.org/10.1007/s10008-024-05894-7

17. Mashkoor F, Shoeb M, Khan JA, Gondal MA, Jeong C (2024) Chemical reduction-induced defect-rich and synergistic effects of reduced graphene oxide based Cu-doped NiO nanocomposite (RGO@ Cu-NiO NCs) decorated on woven carbon fiber for supercapacitor device and their charge storage mechanism. J Energy Storage 104:114578. https://doi.org/10.1016/j.est.2024.114578

18. Gandouzi M, Alshammari AS, Bouzidi M, Khan Z, Mohamed M, Nasrallah TB (2023) DFT study of structural optoelectronic and thermoelectric properties of CuNiO ferromagnetic alloys. Phys Scr 98(7):075936. https://doi.org/10.1088/1402-4896/acdd2e

19. Li R-s, Xin D-q, Huang S-q, Wang Z-j, Huang L, Zhou X-h (2018) A full potential all-electron calculation on electronic structure of NiO. Chin J Phys 56(6):2829–2836. https://doi.org/10.1016/j.cjph.2018.08.022

20. Anisimov VI, Aryasetiawan F, Lichtenstein A (1997) First-principles calculations of the electronic structure and spectra of strongly correlated systems: the LDA+ U method. J Phys Condens Matter 9(4):767. https://doi.org/10.1088/0953-8984/9/4/002

21. Moskvin A (2016) DFT, L (S) DA, LDA+ U, LDA+ DMFT,…, whether we do approach to a proper description of optical response for strongly correlated systems? Opt Spectrosc 121:467–477. https://doi.org/10.1134/S0030400X16100167

22. Kumbhar MB, Chandak VS, Kulal PM (2025) Enhanced ammonia gas sensing performance at room temperature of binder-free NiO, Cu and Co-doped NiO thin films synthesized via the SILAR method. Mater Chem Phys 329:130065. https://doi.org/10.1016/j.matchemphys.2024.130065

23. Kumbhar MB, Patil VV, Chandak VS, Shaikh SB, Chitare YM, Gunjakar JL, Kulal PM (2024) Exploring copper-doped nickel oxide as a superior cathode electrode material for flexible hybrid solid-state supercapacitor device. J Ind Eng Chem 147:422–435. https://doi.org/10.1016/j.jiec.2024.12.032

24. Benrezgua E, Deghfel B, Mahroug A, Yaakob MK, Boukhari A, Amari R, Kheawhom S, Mohamad AA (2021) Experimental and theoretical studies on structural, morphological, electronic, optical and magnetic properties of Zn1-xCuxO thin films (0≤x≤0.125). Mater Sci Semicond Process 134:106012. https://doi.org/10.1016/j.mssp.2021.106012

25. Touhami H, Almi K, Lakel S (2024) Experimental and theoretical investigation of the effect of alkali (Li, Na and K) doping on the properties of nickel oxide thin films: comparative study. Main Group Chem 23(1):73–88. https://doi.org/10.3233/mgc-220130

26. Yeşiltepe Özcelik D, Ebin B, Stopic S, Gürmen S, Friedrich B (2022) Mixed oxides NiO/ZnO/Al2O3 synthesized in a single step via ultrasonic spray pyrolysis (USP) method. Metals 12(1):73. https://doi.org/10.3390/met12010073

27. Mohamed N, Örnek C, Timur S, Uergen M (2022) Anodic behavior of nickel in sub-molten KOH and its relevance for the production of electroactive nickel oxides. Surf Interface 31:101963. https://doi.org/10.1016/j.surfin.2022.101963

28. Ghorui K, Sarkar R, Tudu B (2023) Effect of precursor concentration on structural and optical properties of nickel oxide nanoparticles synthesized by facile sol-gel method. Materials Today: Proceedings. https://doi.org/10.1016/j.matpr.2023.08.259

29. Vidhya M, Sumathi N, Sadaiyandi K, Rajapandi P, Elumalai K, Arunkumar S, Mary AN, Marnadu R, Khan FS, Shkir M (2024) Effect of molar concentration on optoelectronic properties of NiO nanoparticles for p-n junction diode application. Sens Actuators A Phys. https://doi.org/10.1016/j.sna.2023.114995

30. Amari R, Mahroug A, Boukhari A, Deghfel B, Selmi N (2018) Structural, optical and luminescence properties of ZnO thin films prepared by sol-gel spin-coating method: effect of precursor concentration. Chin Phys Lett. https://doi.org/10.1088/0256-307x/35/1/016801

31. Aljarrah RM, Naamah AM, Alkhayatt AHO (2023) Concentration of spraying solution effect on the structural, morphological and optical properties of NiO thin films. Al-Bahir Journal for Engineering and Pure Sciences 3(2):4. https://doi.org/10.55810/2313-0083.1039

32. Moghe S, Acharya A, Panda R, Shrivastava S, Gangrade M, Shripathi T, Ganesan V (2012) Effect of copper doping on the change in the optical absorption behaviour in NiO thin films. Renew Energy 46:43–48. https://doi.org/10.1016/j.renene.2012.02.028

33. Visweswaran S, Venkatachalapathy R, Haris M, Murugesan R (2020) Structural, morphological, optical and magnetic properties of sprayed NiO thin films by perfume atomizer. Appl Phys A Mater Sci Process 126(7):524. https://doi.org/10.1007/s00339-020-03709-w

34 Taşdemirci TÇ (2020) Synthesis of copper-doped nickel oxide thin films: structural and optical studies. Chem Phys Lett 738:136884. https://doi.org/10.1016/j.cplett.2019.136884

35. Ghougali M, Belahssen O, Chala A (2016) Structural, optical and electrical properties of NiO nanostructure thin film. Журнал нано-та електронної фізики 8(2):1–4. 21272/jnep.8(4(2)).04059

36. Anandh Jesuraj S M H, Immanuel P (2013) Structural and optical properties of pure nio and li-doped nickel oxide thin films by sol-gel spin coating method. Int J Sci Res (IJSR)

37. Mohsin MH, Haider MJ, Al-Shibaany ZYA, Haider AJ, Mehadi RO (2021) Synthesis of NiO/Si using sol-gel as a photosensor. Silicon 14(4):1349–1355. https://doi.org/10.1007/s12633-020-00872-w

38. Patil VP, Pawar S, Chougule M, Godse P, Sakhare R, Sen S, Joshi P (2011) Effect of annealing on structural, morphological, electrical and optical studies of nickel oxide thin films. J Surf Eng Mater Adv Technol 01(02):35–41. https://doi.org/10.4236/jsemat.2011.12006

39. Hajer T. Hashim M M M, Souad G. Khalil, Ghassan A. Naeem (2022) Preparation Nanostructured of Cu-Doped NiO Thin Films Using Spin Coating Method for Gas Sensors Applications. J Nanostruct 12: 882–891. https://doi.org/10.22052/JNS.2022.04.010.

40. Jlassi M, Sta I, Hajji M, Ezzaouia H (2014) Optical and electrical properties of nickel oxide thin films synthesized by sol–gel spin coating. Mater Sci Semicond Process 21:7–13. https://doi.org/10.1016/j.mssp.2014.01.018

41. Kim KH, Takahashi C, Abe Y, Kawamura M (2014) Effects of Cu doping on nickel oxide thin film prepared by sol–gel solution process. Optik 125(12):2899–2901. https://doi.org/10.1016/j.ijleo.2013.11.074

42. Mahmoud S, Akl A, Kamal H, Abdel-Hady K (2002) Opto-structural, electrical and electrochromic properties of crystalline nickel oxide thin films prepared by spray pyrolysis. Phys B 311(3–4):366–375. https://doi.org/10.1016/S0921-4526(01)01024-9

43. Hashim HT, Mutter MM, Khalil SG, Naeem GA (2022) Preparation nanostructured of Cu-doped NiO thin films using spin coating method for gas sensors applications. J Nanostruct 12(4):882–891. https://doi.org/10.22052/JNS.2022.04.010

44. Haider AJ, Al- Anbari R, Sami HM, Haider MJ (2019) Enhance preparation and characterization of nickel-oxide as self-cleaning surfaces. Energy Procedia 157:1328–1342. https://doi.org/10.1016/j.egypro.2018.11.298

45. Arif M, Shkir M, Ganesh V, Singh A, Algarni H, AlFaify S (2019) A significant effect of Ce-doping on key characteristics of NiO thin films for optoelectronics facilely fabricated by spin coater. Superlattices Microstruct 129:230–239. https://doi.org/10.1016/j.spmi.2019.03.025

46. Boubaker K (2011) A physical explanation to the controversial Urbach tailing universality. Eur Phys J Plus 126(1):10. https://doi.org/10.1140/epjp/i2011-11010-4

47. Anyaegbunam FNC, Augustine C (2018) A study of optical band gap and associated urbach energy tail of chemically deposited metal oxides binary thin films. Dig J Nanomater Biostruct 13:847–856

48. Vivekanandan J, Usha KS, Sivakumar R, Sanjeeviraja C (2023) Influence of tungsten oxide concentration on structural, morphological, compositional, linear and non-linear optical properties, and vibrational properties on NiO:WO3 thin films. Opt Mater 144:114313. https://doi.org/10.1016/j.optmat.2023.114313

49. Diha A, Benramache S, Benhaoua B (2018) Transparent nanostructured Co doped NiO thin films deposited by sol-gel technique. Optik 172:832–839. https://doi.org/10.1016/j.ijleo.2018.07.062

50. Nayek AK, Luitel H, Haldar B, Sanyal D, Chakrabarti M (2020) Ferromagnetic property of copper doped ZnO: a first-principles study. Comput Condens Matter 23:e00455. https://doi.org/10.1016/j.cocom.2020.e00455

51. Benrezgua E, Deghfel B, Mahroug A, Yaakob MK, Boukhari A, Amari R, Kheawhom S, Mohamad AA (2021) Experimental and theoretical studies on structural, morphological, electronic, optical and magnetic properties of Zn1-xCuxO thin films (0≤ x≤ 0.125). Mater Sci Semicond Process 134:106012. https://doi.org/10.1016/j.mssp.2021.106012

52. Li Y, Yang F, Yu Y (2017) LSDA+ U study on the electronic and anti-ferromagnetic properties of Ni-doped CuO and Cu-doped NiO. Chin J Catal 38(5):767–773. https://doi.org/10.1016/S1872-2067(17)62796-7

53. Yadav A, Chavan UJ, Singh VNJPT (2024) Electrochemical performance of cobalt-doped NiO thin films synthesized by spray pyrolysis. Phase transitions 97(10):710–721. https://doi.org/10.1016/S1872-2067(17)62796-7

54. Sun H, Liao MH, Chen SC, Li ZY, Lin PC, Song SM (2018) Synthesis and characterization of n-type NiO: Al thin films for fabrication of pn NiO homojunctions. J Phys D Appl Phys 51(10):105109

55. Gupta P, Dutta T, Mal S, Narayan J (2012) Controlled p-type to n-type conductivity transformation in NiO thin films by ultraviolet-laser irradiation. J Appl Phys 111(1):3671412. https://doi.org/10.1063/1.3671412

56. Oh S, Jun Y-K, Kim N-H (2025) Magnetron-sputtered and rapid-thermally annealed NiO: Cu thin films on 3D porous substrates for supercapacitor electrodes. Energies 18(11):2704. https://doi.org/10.3390/en18112704

57. Zhang Y-D, Zhao LJ (2019) Enhanced electroluminescence performance of all-inorganic quantum dot light-emitting diodes: a promising candidate for hole transport layer of Cu-doped NiO nanocrystals. J Mater Res 34(16):2757–2764. https://doi.org/10.1557/jmr.2019.130

58. Sathishkumar K, Shanmugam N, Kannadasan N, Cholan S, Viruthagiri GJJ (2015) Synthesis and characterization of Cu $^{2+}$ doped NiO electrode for supercapacitor application. Journal of Sol-Gel Science and Technology. 74:621–630. https://doi.org/10.1007/s10971-015-3641-4

59. Yan H, Zhang D, Xu J, Lu Y, Liu Y, Qiu K, Zhang Y, Luo Y (2014) Solution growth of NiO nanosheets supported on Ni foam as high-performance electrodes for supercapacitors. Nanoscale Res Lett 9(1):424

60. Yadav A, Chavan UJ, Singh VN (2024) Electrochemical performance of cobalt-doped NiO thin films synthesized by spray pyrolysis. Phase Transit 97(10):710–721. https://doi.org/10.1080/01411594.2024.2417223

61. El Nady J, Shokry A, Khalil M, Ebrahim S, Elshaer A, Anas M (2022) One-step electrodeposition of a polypyrrole/NiO nanocomposite as a supercapacitor electrode. Sci Rep 12(1):3611. https://doi.org/10.1038/s41598-022-07483-y

62. Chan X-H, Jennings JR, Hossain MA, Yu KKZ, Wang Q (2011) Characteristics of p-NiO thin films prepared by spray pyrolysis and their application in CdS-sensitized photocathodes. J Electrochem Soc 158(7):H733. https://doi.org/10.1149/1.3590742

63. Brioual B, El-Habib A, Rossi Z, Aouni A, Addou M, Diani M, Allah RF, Jbilou M (2025) Effect of zirconium doping on structural, optical, and electrochemical properties of NiO thin films: electrochromic application. Next Materials 6:100314. https://doi.org/10.1016/j.nxmate.2024.100314

64. Haider S, Abid R, Murtaza I, Shuja A (2023) Unleashing enhanced energy density with PANI/NiO/graphene nanocomposite in a symmetric supercapacitor device, powered by the hybrid PVA/Na2SO4 electrolyte. ACS Omega 8(48):46002–46012. https://doi.org/10.1021/acsomega.3c06900

65. Dhas SD, Maldar PS, Patil MD, Nagare AB, Waikar MR, Sonkawade RG, Moholkar AV (2020) Synthesis of NiO nanoparticles for supercapacitor application as an efficient electrode material. Vacuum 181:109646. https://doi.org/10.1016/j.vacuum.2020.109646

66. Sathishkumar K, Shanmugam N, Kannadasan N, Cholan S, Viruthagiri G (2015) Synthesis and characterization of Cu 2+ doped NiO electrode for supercapacitor application. J Sol-Gel Sci Technol 74:621–630. https://doi.org/10.1007/s10971-015-3641-4

67. Mala NA, Dar MA, Rather MUD, Reshi BA, Sivakumar S, Batoo KM, Ahmad Z (2023) Supercapacitor and magnetic properties of NiO and manganese-doped NiO nanoparticles synthesized by chemical precipitation method. J Mater Sci Mater Electron 34(6):505